

Observability and Synchronization of Neuron Models

LUIS A. AGUIRRE, LEONARDO L. PORTES

Departamento de Engenharia Eletrônica, Programa de Pós Graduação em
Engenharia Elétrica da Universidade Federal de Minas Gerais, Av. Antônio Carlos,
6627, 31.270-901 Belo Horizonte, MG, Brazil.
aguirre@ufmg.br, ll.portes@gmail.com

CHRISTOPHE LETELLIER

Université de Rouen, CNRS, CORIA, UMR 6614, Campus Univ. Madrillet,
F-76800 St Etienne, France. christophe.letellier@atomosyd.net

Abstract

Observability is the property that enables to distinguish two different locations in n -dimensional state space from a reduced number of measured variables, usually just one. In high-dimensional systems it is therefore important to make sure that the variable recorded to perform the analysis conveys good observability of the system dynamics. In the case of networks composed of neuron models, the observability of the network depends nontrivially on the observability of the node dynamics and on the topology of the network. The aim of this paper is twofold. First, a study of observability is conducted using four well-known neuron models by computing three different observability coefficients. This not only clarifies observability properties of the models but also shows the limitations of applicability of each type of coefficients in the context of such models. Second, a multivariate singular spectrum analysis (M-SSA) is performed to detect phase synchronization in networks composed by neuron models. This tool, to the best of the authors' knowledge has not been used in the context of networks of neuron models. It is shown that it is possible to detect

phase synchronization i) without having to measure all the state variables, but only one from each node, and ii) without having to estimate the phase.

1 Introduction

Since the early days of last century there has been sustained activity in developing mathematical models for neuron dynamics. More recently such models have been combined in networks in order to investigate collective behavior. In either approaches mathematical tools and concepts abound, as reviewed by [Siettos and Starke \(2016\)](#), who argue that there must be a continued effort in using such tools to reveal so many aspects of the brain dynamics which remain not understood. The same point had been argued by Brown in a very interesting discussion ([Brown, 2014](#)).

In this respect, an important concept is that of observability of the dynamics from a given measured variable. Since it is not practical, especially in high-dimension systems, to record all state variables, a relevant problem is to know which are the best variables to record to be able to infer the state of the whole system. Observability, although not in its classical interpretation, provides an answer to that question. It has been acknowledged that to choose variables that provide good observability of the dynamics enables estimating the state of a network of neuron models using Kalman-related methods ([Sedigh-Sarvestani et al., 2012](#); [Schiff, 2012](#)). In a recent study about controllability and observability of network motifs built with neuron models, it has been found that “it is necessary to take the node dynamics into consideration when selecting the best driver (sensor) node to modulate (observe) the whole network activity” ([Su et al., 2017](#), Sec. III-A).

In view of this, one of the aims of this paper is to conduct a study of observability properties of four neuron models following three points of view: using the model equations and numerical analysis ([Letellier et al., 2005](#)), using the model equations and symbolic manipulations ([Letellier and Aguirre, 2009](#)) and using time series data ([Aguirre and Letellier, 2011](#)). An interesting point that has been revealed in this study is related to aspects that are specific to neuron models. For instance, in the case of the Hodgkin-Huxley model, three of the four state variables are not directly measurable. The study of observability could help understand if there are any serious limitations related to this. In such a case the use of observability coefficients estimated from data is most convenient, because the practical relevance of measuring ionic currents could be evaluated. Due to the functional relation of such currents with the state variables, the computation of observability coefficients from the equations is significantly more difficult. Other examples are the integrate and fire models, that produce discontinuities in the data. Such phenomenon may have adverse effects on data-driven observability coefficients, and the equation-based

computation of coefficients is also questionable because of the “hidden state variable” related to the firing process. These aspects, that have come to light in the context of the investigated neuron models, are here described for the first time.

Another important aspect that has gained considerable attention is that of synchronization of networked neuron models. Because in real life neurons are not identical and coupling could be weak, phase synchronization is somewhat more well suited than complete synchronization in this context. A difficulty with most procedures used to detect phase synchronization is the need for defining a phase, which is not always simple, if at all possible. Spectral coherence related measures of phase synchronization have recently been considered and found to deviate considerably from expected results (Lowet et al., 2016). An alternative procedure that does not require the estimation of the phase is the multivariate spectrum analysis for phase synchronization phenomena, originally proposed by Groth and Ghil (Groth and Ghil, 2011). This method will be reviewed and applied to detect phase synchronization in networks of neuron models in this work for the first time, to the best of the authors’ knowledge. Although observability and synchronizability are different problems and treated as such in this paper, there is a connection between them in the context of multivariate spectrum analysis, as will be pointed out.

This paper is organized as follows. For the sake of completion, there are two sections with background material. Section 2 briefly describes four of the neuron models considered in this study. Section 3 reviews the main tools used: three different measures of observability and the multivariate singular spectrum analysis, used in detecting phase synchronization. The numerical results concerning observability of the investigated neuron models are presented in Sec. 4 and the results regarding synchronization are briefly described in Sec. 5. Conclusions are provided in Sec. 6.

2 Neuron Models

This section surveys four neuron models presented in chronological order. This choice is admittedly *ad hoc* but it is believed that some of the more commonly used neuron models are included. In presenting the equations, the symbols used in the original publications have been maintained whenever possible. A general comparison of the models used in this paper and many other is provided in (Izhikevich, 2004).

2.1 Hodgkin-Huxley Model

In 1952, Alan Hodgkin and Andrew Huxley published a series of four papers that concluded with a biophysically-based model of neuron dynamics, known as the

Hodgkin-Huxley model ([Hodgkin and Huxley, 1952](#)):

$$\begin{cases} \dot{V} = \frac{1}{C_m} (I - I_K - I_{Na} - I_l) \\ \dot{n} = \alpha_n(1 - n) - \beta_n n \\ \dot{m} = \alpha_m(1 - m) - \beta_m m \\ \dot{h} = \alpha_h(1 - h) - \beta_h h, \end{cases} \quad (1)$$

where

$$\begin{aligned} I_K &= \bar{g}_K n^4 (V - V_K), \quad I_{Na} = \bar{g}_{Na} m^3 h (V - V_{Na}), \quad I_l = \bar{g}_l (V - V_l) \\ \alpha_n &= \frac{0.01(V + 10)}{e^{\frac{V+10}{10}} - 1}, \quad \beta_n = 0.125 e^{\frac{V}{80}} \\ \alpha_m &= \frac{0.1(V + 25)}{e^{\frac{V+25}{10}} - 1}, \quad \beta_m = 4 e^{\frac{V}{18}} \\ \alpha_h &= 0.07 e^{\frac{V}{20}}, \quad \beta_h = \left[e^{\frac{V+30}{10}} + 1 \right]^{-1}, \end{aligned}$$

with the following parameter values: membrane capacitance $C_m = 1 \mu\text{F}/\text{cm}^2$; constant membrane potentials $V_K = 12 \text{ mV}$, $V_{Na} = -115 \text{ mV}$, $V_l = -10.6 \text{ mV}$; constants associated with membrane conductances $\bar{g}_K = 36 \text{ mS}/\text{cm}^2$, $\bar{g}_{Na} = 120 \text{ mS}/\text{cm}^2$ and the conductance $\bar{g}_l = 0.3 \text{ mS}/\text{cm}^2$. I is the total current density through the membrane, and I_K , I_{Na} and \bar{g}_l correspond to the current density due to potassium ions, sodium ions and other ions, respectively. All current densities are given in $\mu\text{A}/\text{cm}^2$. Variables n , m and h are dimensionless variables corresponding to the proportion of the potassium inside of the membrane, the proportion of activating molecules within the membrane, and the proportion of inactivating molecules outside of it, respectively.

2.2 FitzHugh-Nagumo Model

In 1961 Richard FitzHugh published a model obtained from the van der Pol's equation ([FitzHugh, 1961](#)):

$$\begin{cases} \dot{x} = c(y + x - x^3/3 + I) \\ \dot{y} = -(x - a + by)/c, \end{cases} \quad (2)$$

where (a, b, c) are constant parameters and I is a stimulus, that corresponds to membrane current in the Hodgkin-Huxley model. x is usually identified with membrane potential, and y is the recovery variable. In the following year, Jin-Ichi Nagumo and colleagues published an electronic implementation of model (2) that used tunnel diodes ([Nagumo et al., 1962](#)), hence (2) is often referred to as the FitzHugh-Nagumo model ([Schiff, 2012](#)) and it is considered to be a simplified version of the

Hodgkin-Huxley model in the sense that it reproduces some of the main features of the dynamics.

Model (2) with $(a, b, c) = (0.7, 0.8, 3)$ was investigated in (FitzHugh, 1961) with $I = -0.4$ and in (Voos et al., 2004) with $I(t)$ being a slowly varying stimulus within the range $-1.5 \leq I(t) \leq -0.4$.

2.3 Hindmarsh-Rose Model

In 1984 Hindmarsh and Rose provided a modification to a previous model published by them in 1982 thus yielding the following equations for a three-equilibrium-point model with adaptation (Hindmarsh and Rose, 1984)

$$\begin{cases} \dot{x} = y - ax^3 + bx^2 + I - z \\ \dot{y} = c - dx^2 - y \\ \dot{z} = r[s(x - x_1) - z], \end{cases} \quad (3)$$

with $(a, b, c, d) = (1, 3, 1, 5)$, where x_1 is a constant. The constant parameters r and s determine the dynamical response to a short pulse of depolarizing current. Here x is the membrane potential and y is the recovery variable (as in the FitzHugh-Nagumo model). In this model Hindmarsh and Rose added a third equation, where z is an adaptation current that hyperpolarizes the cell. Similar to y , z quantifies the transport of ions but now through slow channels.

An interesting feature of this model is that the dynamics associated to the z variable are very slow when compared to those of x and y . The authors investigate three values for the current: $I = 0.4$, $I = 2$ and $I = 4$. For $I = 3.25$ a “random” (chaotic) burst structure has been reported.

2.4 Izhikevich’s spiking neuron Model

A simple model that reproduces spiking and bursting behavior of known types of cortical neurons was given by Eugene Izhikevich in 2003. It combines aspects of the Hodgkin-Huxley model and of integrate-and-fire neuron models. The result is a surprisingly simple model that reproduces a rich variety of dynamical regimes. The equations are (Izhikevich, 2003):

$$\begin{cases} \dot{v} = 0.04v^2 + 5v + 140 - u + I_{\text{syn}} \\ \dot{u} = a(bv - u), \end{cases} \quad (4)$$

$$\text{if } v \geq 30 \text{ then } \begin{cases} v \leftarrow c \\ u \leftarrow u + d, \end{cases}$$

where v represents the membrane potential and u represents the membrane recovery variable (a, b, c, d) are constant parameters and I_{syn} accounts for the synaptic or

injected dc currents. Depending on the parameter values, a rich variety of dynamical regimes are possible. For instance $(a, b, c, d) = (0.02, 0.2, -50, 2)$ with $I_{\text{syn}} = 10$ results in chattering (Izhikevich, 2003) and $(a, b, c, d) = (0.2, 2, -56, -16)$ with $I_{\text{syn}} = -99$ results in chaotic firing (Izhikevich, 2004) as evidenced by the first-return map to a Poincaré section (Fig. 1). The fact that a second-order model could produce chaos should not cause surprise because the switching function plays the role of the reinjection mechanism as governed by the third equation of the Rössler system for instance, variables u and v being associated with an oscillator as variable x and y of the Rössler system. Izhikevich’s model is therefore a “truncated” model in the sense that all underlying mechanisms are not explicitly described. In a sense, the state of the switch acts as a “hidden state variable”.

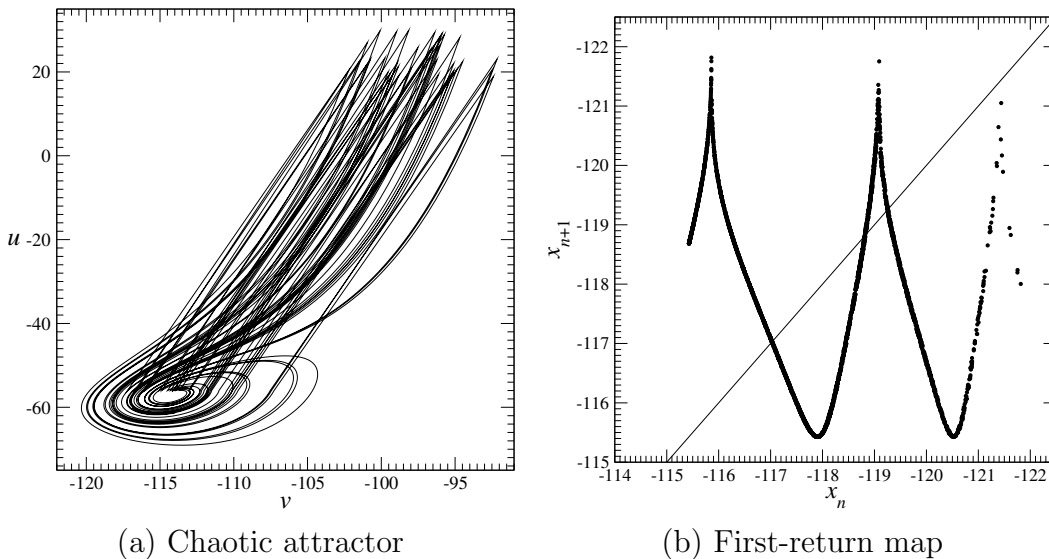


Figure 1: Chaotic behavior produced by the Izhikevich’s model. Parameter values: $(a, b, c, d) = (0.2, 2, -56, -16)$ with $I_{\text{syn}} = -99$. The six-branches first-return map to a Poincaré section of (4) is typical of a “funnel” chaotic behavior encountered in the Rössler system for $a \approx 0.540$, $b = 2$ and $c = 4$.

3 Mathematical and Numerical Tools

In this section we briefly review the observability coefficients and multivariate singular spectrum analysis (M-SSA). Because of confusion in the literature as to the development of observability coefficients (Su et al., 2017), here a brief historical overview is provided.

The concepts of observability and controllability for linear systems are due to Rudolf Kalman (Kalman, 1960). These were extended to nonlinear systems over

a decade later as discussed in (Hermann and Krener, 1977). In both cases such concepts were “yes” or “no” concepts. Bernard Friedland suggested computing a conditioning number of a symmetric matrix obtained from the *linear* observability or controllability matrices as a way of getting a continuous function of the parameters instead of a binary (yes or no) classification (Friedland, 1975). In fact, it was argued that although a similarity transformation of coordinates would not change the rank of the observability or controllability matrices, and therefore would not alter the resulting classification, the indices proposed by Friedland are sensitive to such a transformation (Aguirre, 1995), to changes in parameters and, in the nonlinear case, to the location in state space. The concept of a continuously varying quantification of observability was adapted to nonlinear dynamical systems in (Letellier et al., 1998; Letellier and Aguirre, 2002) where the jacobian matrix *of the vector field* was used in the analysis. Later on, it was shown that the jacobian matrix *of the map* between the original and embedding spaces coincided with the nonlinear observability matrix based on Lie derivatives (Letellier et al., 2005). Hence, the quantification of observability was then performed using such a matrix. The extension to multivariate embeddings and the relation to Takens’ theorem were presented in (Aguirre and Letellier, 2005). The procedure proposed in (Letellier et al., 2005) is briefly reviewed in the next section.

3.1 Numerical observability coefficients

Consider the autonomous system $\dot{\mathbf{x}} = f(\mathbf{x})$, where $\mathbf{x} \in \mathbb{R}^n$ is the state vector and $f : \mathbb{R}^n \mapsto \mathbb{R}^n$ is the vector field. Consider further the measurement function $h : \mathbb{R}^n \mapsto \mathbb{R}$ such that $s(t) = h(\mathbf{x})$, where $s \in \mathbb{R}$ is referred to as the observable or recorded variable. The case for which $s \in \mathbb{R}^p, p > 1$ has been investigated and reported in (Aguirre and Letellier, 2005). Differentiating $s(t)$ with respect to time yields

$$\dot{s}(t) = \frac{d}{dt}h(\mathbf{x}) = \frac{\partial h}{\partial \mathbf{x}} \dot{\mathbf{x}} = \frac{\partial h}{\partial \mathbf{x}} \mathbf{f}(\mathbf{x}) = \mathcal{L}_f h(\mathbf{x}), \quad (5)$$

where $\mathcal{L}_f h(\mathbf{x})$ is the Lie derivative of h along the vector field \mathbf{f} (Isidori, 1995).

The general observability matrix can be written as (Hermann and Krener, 1977)

$$\mathcal{O}_s(\mathbf{x}) = \begin{bmatrix} \frac{\partial \mathcal{L}_f^0 h(\mathbf{x})}{\partial \mathbf{x}} \\ \vdots \\ \frac{\partial \mathcal{L}_f^{n-1} h(\mathbf{x})}{\partial \mathbf{x}} \end{bmatrix}, \quad (6)$$

where s indicates that $\mathcal{O}_s(\mathbf{x})$ refers to the system observed from $s(t)$. In the case $h(\mathbf{x})$ returns only one of the state variables matrix (6) can be rewritten as

$$\mathcal{O}_s(\mathbf{x}) = \begin{bmatrix} C \\ C\tilde{A} \\ \vdots \\ C\tilde{A}^{n-1} \end{bmatrix}, \quad (7)$$

where $C = [1 \ 0 \ \dots \ 0]$ if $h(\mathbf{x})$ returns the first state variable, $C = [0 \ 1 \ 0 \ \dots \ 0]$ if $h(\mathbf{x})$ returns the second, and so on. Also

$$\tilde{A}^{j+1} = \left[\frac{\partial \mathcal{L}_f^j f_i(\mathbf{x})}{\partial \mathbf{x}} \right], \quad i = 1, 2, \dots, n \quad (8)$$

for $j = 0, \dots, n - 2$, where

$$\mathcal{L}_f f_i(\mathbf{x}) = \frac{\partial f_i(\mathbf{x})}{\partial \mathbf{x}} \mathbf{f}(\mathbf{x}) = \sum_{k=1}^n \frac{\partial f_i(\mathbf{x})}{\partial x_k} f_k \quad (9)$$

is the Lie derivative of the i th component of the vector field \mathbf{f} and the higher-order derivatives can be recursively determined as

$$\mathcal{L}_f^j f_i(\mathbf{x}) = \mathcal{L}_f [\mathcal{L}_f^{j-1} f_i(\mathbf{x})], \quad (10)$$

with $\mathcal{L}_f^0 f_i(\mathbf{x}) = f_i(\mathbf{x})$. If $\mathcal{O}_s(\mathbf{x})$ is singular then there is no global diffeomorphism between the original phase space and the n -dimensional space reconstructed using s and $n - 1$ successive derivatives of it. Because the system is nonlinear, often $\mathcal{O}_s(\mathbf{x})$ may become singular or nearly singular at specific regions of state space at which the original dynamics become poorly observable or nonobservable altogether.

Hence it is sometimes instructive to have an average measure of the numerical conditioning of $\mathcal{O}_s(\mathbf{x})$. This is achieved by first computing along a trajectory $\mathbf{x}(t)$

$$\delta_s(\mathbf{x}) = \frac{|\lambda_{\min}[\mathcal{O}_s(\mathbf{x})^T \mathcal{O}_s(\mathbf{x})]|}{|\lambda_{\max}[\mathcal{O}_s(\mathbf{x})^T \mathcal{O}_s(\mathbf{x})]|}, \quad (11)$$

where $\lambda_{\max}[\cdot]$ indicates the maximum eigenvalue of the argument estimated at point $\mathbf{x}(t)$ (likewise for λ_{\min}); $0 \leq \delta(\mathbf{x}) \leq 1$, and the lower bound is reached when the system is not observable at point \mathbf{x} . Finally, averaging $\delta_s(\mathbf{x})$ along a trajectory over the interval $t \in [0; T]$ yields

$$\delta_s = \frac{1}{T} \sum_{t=0}^T \delta_s(\mathbf{x}(t)), \quad (12)$$

where T is the final time considered and, without loss of generality, the initial time was set to be $t = 0$.

3.2 Symbolic Observability Coefficients

The advantage of the numerical observability coefficients is that they take into account the domain of the state space actually visited by the trajectory and, consequently, whether the neighborhood of the singular observability manifold is visited or not. Nevertheless, these observability coefficient are not normalized and cannot be used to compare different dynamical systems. To overcome such a problem, symbolic observability coefficients were introduced (Letellier and Aguirre, 2009). The underlying idea is that the more complicated the determinant $\det \mathcal{O}_s$ of the observability matrix, the less observable. Although the analytical computation of $\det \mathcal{O}_s$ can be a nearly impossible task for a five-dimensional rational system, the complexity of $\det \mathcal{O}_s$ can be assessed simply by counting the number of linear, nonlinear and rational terms in it, without paying attention to its exact form (Bianco-Martinez et al, 2015). This is computed from the Jacobian matrix of the system which is transformed into symbolic form, using 1 , $\bar{1}$, and $\bar{\bar{1}}$ for linear, nonlinear and rational elements, respectively. The observability matrix is then constructed using symbolic algebra detailed in (Bianco-Martinez et al, 2015). The symbolic observability coefficient is thus defined as

$$\eta_{s^n} = \frac{N_1}{N_1 + N_{\bar{1}} + N_{\bar{\bar{1}}}} + \frac{N_{\bar{1}}}{(\max(N_1, 1) + N_{\bar{1}} + N_{\bar{\bar{1}}})^2} + \frac{N_{\bar{\bar{1}}}}{(\max(N_1, 1) + N_{\bar{1}} + N_{\bar{\bar{1}}})^3}, \quad (13)$$

where N_1 , $N_{\bar{1}}$ and $N_{\bar{\bar{1}}}$ are the numbers of symbolic terms 1 , $\bar{1}$ and $\bar{\bar{1}}$, respectively. These symbolic coefficients are very promising for assessing the observability of large systems and networks (Letellier et al, 2017). According to (Sendiña-Nadal et al., 2016), the observability can be considered “good” when $\eta_{s^3} > 0.75$, meaning that most likely the determinant of the observability matrix is linear if not constant; consequently the influence of the singular observability matrix is not very important.

3.3 Observability coefficients from data

The procedures reviewed in Sec. 3.1 and Sec. 3.2 require the knowledge of the system equations. Motivated by the fact that in practice equations are not always available, an alternative procedure was proposed in (Aguirre and Letellier, 2011). However, observability is, by definition, related to the equations of the vector field. Hence estimating coefficients from data is only an indirect way of assessing observability from some of its *signatures* found in a reconstructed (embedding) space, as explained next.

The rationale behind the method in (Aguirre and Letellier, 2011) is that in the embedding space of a system with poor observability conveyed by a recorded time series, trajectories are either pleated or squeezed. Such features result in a more complex *local* structure in the embedding space. On the other hand, in the space reconstructed using good observables, very often, trajectories are unfolded comfortably and that translates into a more simple local structure of such a space. The SVDO coefficients hence quantify, using the singular value decomposition (SVD) of a trajectory matrix, the local complexity of the reconstructed space. Simpler structures are associated with better observability whereas more complex local structures with poorer observability. A key point to be noticed here is that SVDO cannot quantify observability *per se*, which by definition would require the vector field equations, but rather are indicators of the *average local complexity* of a reconstructed space, which often – but not always, as will be seen shortly – correlates with observability.

This procedure assumes that the embedding space is reasonable, in the sense that the dimension and delay time – in the case of time delay coordinates – have been correctly chosen. Hence if trajectories are either pleated or squeezed this is attributed to poor observability rather than to a bad choice of embedding parameters. In this paper we use time delay coordinates. Although the results will be reported for a given time delay and embedding dimension, numerical studies with different values of such parameters show no change in the ranking of the variables in terms of observability.

3.4 Multivariate singular spectrum analysis

Here, the use of the structured-varimax multivariate spectrum analysis (svM-SSA) for phase synchronization phenomena, originally proposed by Groth and Ghil (Groth and Ghil, 2011), is briefly reviewed (for a full discussion of the method, along with the introduction of a Monte Carlo based statistical confidence test, see (Groth, 2015)). Recently, it was argued that the explanatory power of svM-SSA on the mechanism of phase synchronization is greatly enhanced by the use of a single state variable, as compared to the original approach using all of them, as long as this variable provides good observability of the dynamics as compared to the rest (Portes and Aguirre, 2016a).

Consider J coupled oscillators and the respective time series of length N of the variable that provides the best observability. Each time series is split in windows of m -data points (Broomhead and King, 1986), and a full augmented “trajectory matrix” $\mathbf{X} = [\mathbf{X}_1, \dots, \mathbf{X}_J] \in \mathbb{R}^{N-m+1, Jm}$ is formed by concatenating the individual time series. In the M-SSA literature, the parameter m is called window width or embedding dimension: we prefer to use the former term. The svM-SSA starts

by the eigendecomposition of the covariance matrix $\mathbf{C} = \mathbf{X}^T\mathbf{X}/(N - m + 1)$ as $\mathbf{\Lambda} = \mathbf{E}^T\mathbf{C}\mathbf{E}$. To overcome a known mixture of the eigenvectors related to the individual subsystems, a structured-varimax rotation (Groth and Ghil, 2011; Portes and Aguirre, 2016b) is performed on the first S eigenvectors, $\mathbf{E}_S^* = \mathbf{E}_S\mathbf{T}$. Finally, the modified variances $\{\lambda_k^*\}_{k=1}^S \equiv \text{diag}(\mathbf{\Lambda}_S^*)$ are obtained through $\mathbf{\Lambda}_S^* = \mathbf{T}^T\mathbf{\Lambda}_S\mathbf{T}$ and they encode information about the underlying structure of the data: a single high value is related to a trend; pairs of nearly equal values reflect oscillatory modes; near zero values are associated with noncoherent oscillations and will be referred to as the noise floor. Hence it is possible to infer about phase synchronization, *without any prior definition* of how to estimate the oscillators phases, from the evolution of λ_k^* pairs associated to the oscillatory modes in the data, as schematically illustrated in Fig. 2 for $J = 4$ idealized oscillators.

4 Results on Observability

Here we provide numerical results about the observability of the models in Section 2 which were integrated using a 4th-order Runge-Kutta algorithm with integration step $h = 0.01$.

4.1 Hodgkin-Huxley Model

Given the complexity and dimension of the Hodgkin-Huxley model, the observability matrices are too large to be shown here. Also, since (1) is a biophysically-based model, when investigating observability properties one should keep in mind what variables are actually recordable. Out of the four state variables of this model only the membrane potential V is recordable, the other variables being dimensionless quantities. Nonetheless, for the sake of completion, we here report the observability coefficients for the four state variables: $\delta_V = 1.1122 \cdot 10^{-7}$, $\delta_n = 1.0872 \cdot 10^{-6}$, $\delta_m = 5.1427 \cdot 10^{-9}$ and $\delta_h = 4.8986 \cdot 10^{-6}$. The symbolic Jacobian matrix is

$$\mathcal{J}^{\text{sym}} = \begin{bmatrix} \bar{1} & \bar{1} & \bar{1} & \bar{1} \\ \bar{1} & \bar{1} & 0 & 0 \\ \bar{1} & 0 & \bar{1} & 0 \\ \bar{1} & 0 & 0 & \bar{1} \end{bmatrix} \quad (14)$$

from which the symbolic observability coefficients $\eta_{V^4} = 0.12$, and $\eta_{n^4} = \eta_{m^4} = \eta_{h^4} = 0.19$ can be obtained.

Because the state variables n , m and h cannot be measured, a different procedure was followed that is made available by using the indirect assessment of observability from data proposed in (Aguirre and Letellier, 2011). Hence the membrane potential

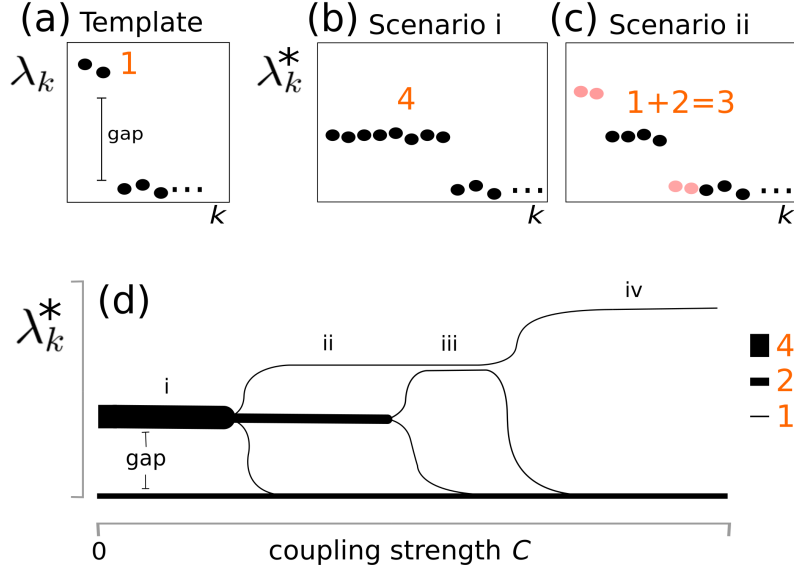


Figure 2: Schematic representation of an svM-SSA for $J = 4$ idealized coupled oscillators. (a) The *template*, shows the signature of a single oscillatory mode, identified by a unique ($\mu = 1$) pair of singular values λ_k separated from the “noise floor” by a clear gap. (b) When the oscillators are not phase synchronized, the svM-SSA shows $\mu = 4$ pairs of *modified variances* λ_k^* (similar to “four concatenated templates”) before a small gap, indicating four distinct oscillatory modes. (c) When two oscillators phase synchronize (PS), the corresponding *single* λ_k pair is larger than the other two associated with the remaining non-synchronized oscillators, hence $\mu = 3$ (before the gap). Note that the increase of λ_k^* for one pair due to the phase synchronization of two oscillators is accompanied by another pair merging with the noise floor (both pairs are indicated in orange). (d) λ_k^* for an increasing coupling strength C : (i) oscillators start non-synchronized – like in (b); (ii) two oscillators forms a PS cluster when a pair of λ_k^* increase and another pair fall to the noise floor – as the orange pairs in (c); (iii) other two oscillators form a second PS cluster, and again there is an increase in a λ_k^* pair while the other merges with the noise floor (and $\mu = 2$); (iv) finally the two clusters merge into a single PS one. The number μ of λ_k^* pairs above the noise floor (equivalently, of different oscillatory modes detected) is indicated by the thickness of the lines.

V and the currents I_K , I_{Na} and I_l were considered as candidate variables to be used in reconstructing a phase space for the dynamics.

In so proceeding, the following SVDO coefficients were found $S_V = 0.109 \pm 0.0009$, $S_{I_K} = 0.093 \pm 0.0015$, $S_{I_{Na}} = 0.054 \pm 0.0024$, $S_{I_l} = 0.167 \pm 0.0028$ for $I = -10$ which show that the best variables for reconstructing a phase space using delay coordinates are V and I_l . From a practical point of view, the best variable to be recorded is probably the potential V as I_l is the ionic current of *all other* ions besides those of potassium and sodium. The reported values were computed using a 5-dimensional embedding space and a common delay time ($\tau = 100$ sampling intervals) for the three variables. The reported values are mean plus-minus one standard deviation over 10 Monte Carlo runs.

4.2 FitzHugh-Nagumo Model

The observability matrix for model (2) when x is recorded is:

$$\mathcal{O}_x = \begin{bmatrix} 1 & 0 \\ -c(x^2 - 1) & c \end{bmatrix}, \quad (15)$$

with determinant $\det(\mathcal{O}_x) = c$, hence unless $c = 0$ the system is observable from the x variable, although observability could be poor for very small values of c . Recording the recovery variable y yields the observability matrix:

$$\mathcal{O}_y = \begin{bmatrix} 0 & 1 \\ -1/c & -b/c \end{bmatrix}, \quad (16)$$

also with constant determinant $\det(\mathcal{O}_y) = 1/c$. Hence for very high values of c , the y variable conveys worse observability of the dynamics.

Figure 3 shows the observability coefficients for the FitzHugh-Nagumo model. Notice that because \mathcal{O}_x depends on variable x it varies along the limit cycle on the x - y plane which, in turn is affected by I . Contrary to this \mathcal{O}_y is constant throughout the phase plane and is not influenced by the stimulus. Both observability coefficients δ_x and δ_y are of the same order of magnitude for the chosen parameters. Hence, unless c is very large or very small, both state variables are comparable in what concerns observability, although measuring y ensures more uniform performance along the limit cycle. The symbolic observability matrix is

$$\mathcal{O}_x^{\text{sym}} = \begin{bmatrix} 1 & 0 \\ \bar{1} & 1 \end{bmatrix} \quad (17)$$

and the corresponding determinant is $\text{Det } \mathcal{O}_x^{\text{sym}} = 1 \otimes 1$ where \otimes is the multiplicative law between the symbols as defined in (Bianco-Martinez et al, 2015); only constant

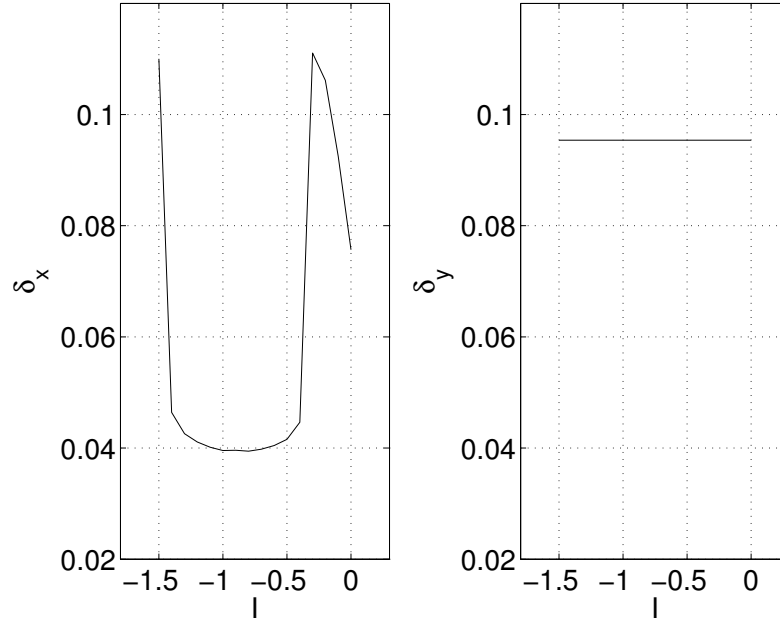


Figure 3: Observability coefficients computed for the FitzHugh-Nagumo model (2). with $(a, b, c) = (0.7, 0.8, 3)$ and the current I was maintained constant for each value in the range $-1.5 \leq I \leq -0.4$.

terms are involved in the symbolic determinant and the corresponding symbolic observability coefficient is therefore $\eta_{x^2} = 1$. As long as c is sufficiently different from 0, the symbolic observability coefficient does not overestimate the observability of the system. With a similar approach, we found $\eta_{y^2} = 1$.

The SVDO for the Fitzhugh-Nagumo model are $S_x = 0.301 \pm 0.0199$, $S_y = 0.206 \pm 0.0058$ for $I = -0.4$ which confirm that the observability of both variables are comparable and that the embedding space reconstructed with y is rather more homogeneous. These values were computed using a 3-dimensional embedding space and a common delay time ($\tau = 100$ sampling intervals) for the three variables. The reported values are mean plus-minus one standard deviation over 10 Monte Carlo runs.

4.3 Hindmarsh-Rose Model

The observability of the HR model has been considered recently in a pair of papers (Portes and Aguirre, 2016a; Sendiña-Nadal et al., 2016). In the first paper a modified version of (3) was considered with linearly transformed coupled equations (Belykh et al., 2005), and in the second symbolic observability coefficients (Letellier and Aguirre, 2009) were computed. So here we compute the observability coefficients

as used in (Letellier et al., 2005) for model (3). Following (Sendiña-Nadal et al., 2016) we use $(a, b, c, d) = (1, 3, 1, 5)$ and $(r, s, x_1, I) = (0.001, 4, -\frac{1+\sqrt{5}}{2}, 3.318)$.

The observability matrices for model (3) are:

$$\mathcal{O}_x = \begin{bmatrix} 1 & 0 & 0 \\ 2bx - 3ax^2 & 1 & -1 \\ O_{31}^x & -3ax^2 + 2bx - 1 & 3ax^2 - 2bx + r \end{bmatrix}, \quad (18)$$

where $O_{31}^x = (2bx - 3ax^2)^2 - rs - 2dx + (2b - 6ax)(-ax^3 + bx^2 + I + y - z)$. \mathcal{O}_x becomes singular for $r = 1$ because in that case the two last columns become linearly dependent (LD), in fact, $\det(\mathcal{O}_x) = r - 1$. Singularity is not expected to happen given the range of values usually used for r , although a negative value for the determinant may indicate that the original and reconstructed spaces are topologically equivalent, but *not* orbitally equivalent, that is the relative direction of trajectories may be different in each space;

$$\mathcal{O}_y = \begin{bmatrix} 0 & 1 & 0 \\ -2dx & -1 & 0 \\ O_{31}^y & 1 - 2dx & 2dx \end{bmatrix}, \quad (19)$$

where $O_{31}^y = -2d(-x - ax^3 + bx^2 + I + y - z) - 2dx(2bx - 3ax^2)$. \mathcal{O}_y becomes singular at $x = 0$, as the last column becomes null, in fact $\det(\mathcal{O}_y) = 4d^2x^2 = 100x^2$, for the parameters used. Although this situation could happen several times during firing, the associated dynamics are so fast that the time the system spends close to $x = 0$ is so short that this does not pose practical observability problems (Frunzete et al., 2012). Finally, the observability matrix when z is recorded is:

$$\mathcal{O}_z = \begin{bmatrix} 0 & 0 & 1 \\ rs & 0 & -r \\ rs(2bx - 3ax^2) - r^2s & rs & r(r - s) \end{bmatrix}, \quad (20)$$

which becomes singular at $rs = 0$. In this case $\rho[\mathcal{O}_z] = 1$, where $\rho[\]$ stands for the rank. This, added to the fact that r is already quite small, shows that z conveys poor observability of the system. It is interesting to notice that although $\det(\mathcal{O}_z) = r^2s^2 = 1.6 \cdot 10^{-5}$ is constant this does not imply good observability.

In order to quantify observability, coefficients were computed and the results shown in Figure 4. As seen, the fast variable provides much better observability than the slow variable z . Values of I around 2 slightly favors y compared to x , but as the current increases x becomes slightly better. This difference might not be critical in practice.

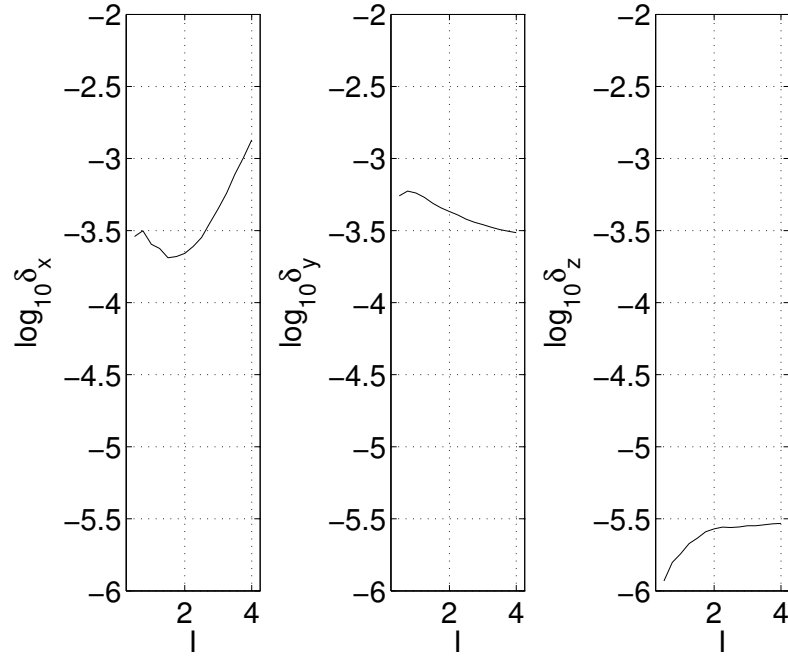


Figure 4: Observability coefficients computed for the Hindmarsh-Rose model. $(a, b, c, d) = (1, 3, 1, 5)$, $(r, s, x_1) = (0.001, 4, -\frac{1+\sqrt{5}}{2})$ and the current was varied within the range $0.5 \leq I \leq 4$. In this plot the logarithm of the coefficients are shown.

The symbolic observability matrix reads

$$\mathcal{O}_x^{\text{sym}} = \begin{bmatrix} 1 & 0 & 0 \\ \bar{1} & 1 & 1 \\ \bar{1} & \bar{1} & \bar{1} \end{bmatrix} \quad (21)$$

and $\eta_{x^3} = 0.25$. Nevertheless, $\det \mathcal{O}_x = r - 1$ and is clearly not dependent on the location in the state space. It is never singular unless $r \neq 1$. A global diffeomorphism could be therefore expected, that is, a full observability should be provided by this variable although it could be very ill-conditioned, and therefore poor. This is one of the rare cases where two nonlinear terms in the computation of the determinant are cancelling each other; the symbolic computation is therefore very different from an analytical computation. Note that as the dimension of the system increases, this situation becomes less likely. It has been argued that from the symbolic point of view, the coefficient η_{x^3} should be corrected to be equal to 1 (Sendiña-Nadal et al., 2016). As long as r is significantly different from 1, taking $\eta_{x^3} = 1$ should be a fair estimation of the observability. From the two other symbolic observability matrix, we obtained $\eta_{y^3} = 0.56$ and $\eta_{z^3} = 1$.

The symbolic observability coefficient η_{x^3} — if not corrected — would suggest a rather poor observability of the dynamics underlying the Hindmarsh-Rose system from variable x . In fact, and contrary to what is provided from the determinant point of view, variable x does not provide a good observability of the underlying dynamics. This is confirmed by a differential embedding induced by variable x of the attractor produced by the Hindmarsh-Rose system (Fig. 5a) which clearly shows that the chaotic nature of the behavior is poorly evidenced, contrary to what is observed when the differential embedding induced by variable z is used (Fig. 5c). Contrary to what was recommended in (Sendiña-Nadal et al., 2016), the symbolic observability coefficient η_{x^3} should *not* be changed since it correctly reveals that observability of the dynamics is, in fact, poor.

The SVDO for this system are $S_x = 0.665 \pm 0.1557$, $S_y = 0.449 \pm 0.1566$ and $S_z = 186.628 \pm 33.6825$, for $I = 3.318$ and $S_x = 0.416 \pm 0.0368$, $S_y = 0.201 \pm 0.0282$ and $S_z = 19.452 \pm 0.6102$ for $I = 2$ (mean plus-minus one standard deviation over 10 Monte Carlo runs). These values were computed using a 4th dimensional embedding space and a common delay time ($\tau = 100$ sampling intervals) for the three variables. Numerical experimentation with other values did not change the ranking of the variables.

For both values of I we find that x and y variables have similar features (as for δ_x and δ_y), but the great difference is that S_z suggests that z provides much better “observability”. This was also the case of the symbolic observability coefficients (if not corrected). The reconstructed attractors — using delay or derivative coordinates —,

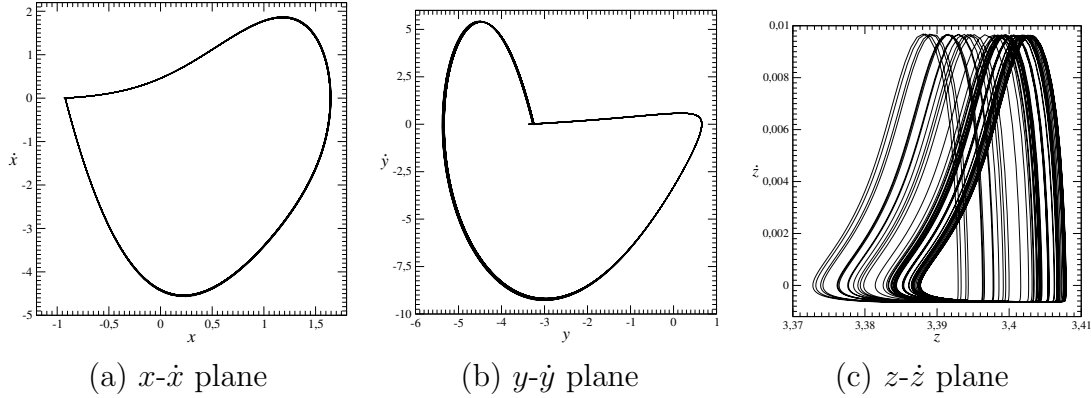


Figure 5: Plane projection of the differential embedding induced by each variable of the Hindmarsh-Rose system.

evidence that the chaotic nature of the behavior produced by the Hindmarsh-Rose model is better evidenced by variable z . The values of the observability coefficient S_s also confirm these results. This does not necessarily mean that z is a good observable. In fact, the fast dynamics (spikes) are practically invisible from z — which corresponds to the flat bottom of the attractor in Figure 5c. In few words it seems that z is the best observable for slow dynamics (and chaos) whereas x and y convey information on the spikes, in the chattering regime.

4.4 Izhikevich’s spiking neuron Model

The observability matrix for model (4) when v is recorded is:

$$\mathcal{O}_v = \begin{bmatrix} 1 & 0 \\ (2v/25) + 5 & -1 \end{bmatrix}, \quad (22)$$

with determinant $\det(\mathcal{O}_v) = -1$. Recording the recovery variable u yields:

$$\mathcal{O}_u = \begin{bmatrix} 0 & 1 \\ ab & -a \end{bmatrix}, \quad (23)$$

also with constant determinant $\det(\mathcal{O}_u) = -ab$. Because \mathcal{O}_u is constant, the observability features do not vary in phase space, unlike for the case when the membrane potential v is measured. In particular, switching v will directly affect \mathcal{O}_v . A peculiar aspect of this model is that both determinants are negative.

$\delta_v = 0.3280$ and $\delta_u = 1.5987 \cdot 10^{-5}$ for $(a, b, c, d) = (0.02, 0.2, -50, 2)$ with $I = 10$, and $\delta_v = 0.3948$ and $\delta_u = 0.1459$ for $(a, b, c, d) = (0.2, 2, -56, -16)$ with $I = -99$. Hence in both scenarios the membrane potential is the variable that provides best observability. More interestingly, the recovery variable is very

poor observability-wise in the chattering regime, whereas it is comparable to the membrane potential in the chaotic regime. By definition, the symbolic observability coefficients are not dependent on the parameter values. We thus found $\eta_u^2 = \eta_v^2 = 1$ (for chattering and chaotic regimes) which would suggest that any of these two variables offers a full observability. It must be clear that by construction this is an approximation to observability since the switching mechanism is not fully described in terms of differential equation (at least a third variable would be necessary for this) and, consequently, there is no available technique so far to rigorously assess the observability of such a system.

The SVDO coefficients ($d_e = 3$ and $\tau = 100$ sampling intervals) for model (4) are $S_v = 0.858 \pm 0.2721$, $S_u = 0.173 \pm 0.1164$ for chattering and $S_v = 0.750 \pm 0.2869$, $S_u = 8.376 \pm 0.5058$ for the chaotic regime. It is worth mentioning that in both analyzes, the observability using the recovery variable improves when the dynamics are chaotic. It should be pointed out that the discontinuities of the trajectories in state space produced by model (4) might have some unknown effect on the computation of the SVDO coefficients. It is the first time that such coefficients are computed from discontinuous data.

It is arguable that observability should not strongly depend on the dynamical regime. This view which is something like “structural observability” is captured by the symbolic coefficients proposed in (Letellier and Aguirre, 2009). On the other hand because the system visits different regions of the state space during different dynamical regimes, and since the observability matrix might become singular at certain places, it can be expected that the dynamical regime might have some influence on observability features.

The results concerning observability are summarized in Table 1.

5 Synchronization in Networks of Neuron Models

In this section, we provide numerical evidence that phase synchronization in networks of neuron models can be detected without estimating the phase, by using the svM-SSA with the single variable approach (see Sec. 3.4). This is viable, and relevant in practice, due to the fact that the variable experimentally measured provides good observability of the system dynamics (Sec. 4).

This is illustrated by three examples, with increasingly complexity. The first explored scenario is a chain of *phase coherent* FitzHugh-Nagumo neuron models. This allows one to compare the svM-SSA results with the one provided by the mean observed frequencies analysis (estimated through the phases of the analytical signal). The second scenario is the synchronization of coupled *bursting* neurons, which represents a challenging system with two very different time scales. For this,

Table 1: Observability coefficients for the different models investigated in this work.

Hodgkin-Huxley model			
	δ_s	η_{s^4}	S_s
V	$1.1122 \cdot 10^{-7}$	0.12	0.109
n	$1.0872 \cdot 10^{-6}$	0.19	0.093
m	$5.1427 \cdot 10^{-9}$	0.19	0.054
h	$4.8986 \cdot 10^{-6}$	0.19	0.167
FitzHugh-Nagumo model			
	δ_s	η_{s^2}	S_s
x	Fig. 3	1.00	0.301
y	0.09	1.00	0.206
Hindmarsh-Rose model			
	δ_s	η_{s^3}	S_s
x	$3.16 \cdot 10^{-4}$	0.25	0.665
y	$3.16 \cdot 10^{-4}$	0.56	0.449
z	$3.16 \cdot 10^{-6}$	1.00	186.630
Izhikevich's model			
	δ_s	η_{s^2}	S_s
u	0.1459	1.00	0.750
v	0.3948	1.00	8.376

we investigate a chain of coupled Hindmarsh-Rose neuron models in the “random” bursting regime. The last example explores the feasibility of the svM-SSA itself in the synchronization analysis of coupled neurons in a *large* network. The svM-SSA provides detailed information of synchronization mechanism (e.g., PS clustering) in small networks, but what kind of information this technique could bring in large ones? This is investigated in the context of a network of 1000 Izhikevich’s spiking neuron models.

5.1 FitzHugh-Nagumo model

Consider a chain of $J = 5$ diffusively coupled FitzHugh-Nagumo neuron models:

$$\begin{cases} \dot{x}_j = c(y + x - \frac{x^3}{3} + z) + C \sum_{i \in \Gamma_j} (x_i - x_j) \\ \dot{y}_j = -(x - a + by)/c \end{cases} \quad (24)$$

with $j = 1, \dots, J$, where C is the coupling strength, and Γ_j is the set of values of i that correspond to the oscillators coupled to j . Along this section, data was generated by integrating (24) with integration step $h = 0.01$ time units for a total time $t_{\text{sim}} = 450$ t.u., using a 4th-order Runge-Kutta algorithm. The first $t_{\text{trans}} = 50$ t.u. were discarded, and the time series of x and y were sampled with sampling time $t_s = 0.7$ t.u. (yielding approximately 15 data points per period). The other parameters were $(a, b) = (0.7, 0.8)$, with a detuning introduced by setting $c_j = c_1 + (j - 1)\Delta c$, with $c_1 = 3$, $\Delta c = 0.2$ and $I = -4$.

Before starting the synchronization analysis, one needs to know the specific “fingerprint” of the oscillatory dynamics of one oscillator in the svM-SSA. Figure 6 shows the power spectrum of the x time series and the 20 leading svM-SSA singular values (the template for svM-SSA) for a single (uncoupled) neuron model ($j = 1$). The signal present several harmonics, with the fundamental frequency at ≈ 0.09 Hz (a period of $T \approx 11$ t.u.). Then, we set the svM-SSA’s window width $m = 31$ ($\approx 2T/t_s$), covering almost two oscillatory periods. The template in Fig. 6(b) shows that a single oscillator will be identified by the svM-SSA as two leading pairs of singular values ($\lambda_{1,2}$ and $\lambda_{3,4}$), which are associated with the two strongest oscillatory modes of the signal.

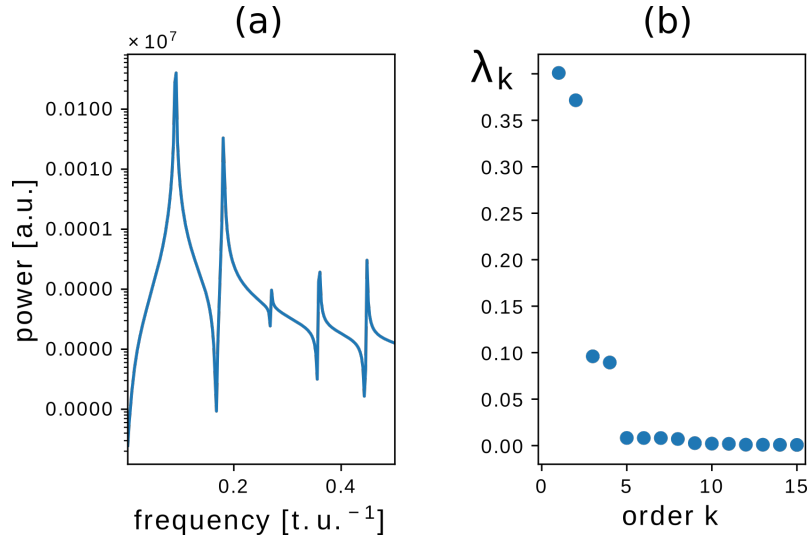


Figure 6: (a) Power spectrum density and (b) svM-SSA template analysis of a FitzHugh-Nagumo neuron. Two oscillatory modes are predominant, a stronger ($\lambda_{1,2}$) and a weaker one ($\lambda_{3,4}$).

We illustrate the use of the svM-SA by investigating the synchronization dynamics of the chain for an increasing coupling strength $C \in [0, 0.06]$. For the sake of clarity, a crosscheck of the results was done by considering the mean frequency lock-

ing $\Omega_j = \Omega_i$ as a (weak) condition for the characterization of PS, and by the visual inspection of the spatiotemporal patterns $x_j(t)$ and $y_j(t)$ (as is usual in neuroscience). The Ω_j were computed through the linear least squares fit of the instantaneous phase $\phi_j(t)$ (estimated through the analytic signal based on the Hilbert transform).

Figure 7 shows the results. The following features are worth noticing. First, at low values of the coupling strength (e.g., at $C = C_1$, first dashed vertical line) the five oscillators have different frequencies Ω , suggesting no PS. Agreeing with that, the svM-SSA is equivalent to the “concatenation” of 5 individual λ templates. Second, the onset of phase synchronization, identified by the mean frequency analysis as $\Omega_3 = \Omega_4$, occurs at C_2 (second dashed vertical line). The svM-SSA captured the onset of PS much earlier, identified by the increasing value of a λ^* pair with a simultaneous drop of other one to the noise floor. Third, several “jumps” are presented in the mean frequency plot, associated with episodes of poor or inappropriate frequency estimates (e.g., due to phase slips), one of them at $C = C_4$. We obtained this result regardless the phase estimate definition used (i.e, $\arctan(y/x)$ or through a Poincaré section, not shown). Since the svM-SSA does not require the computation of phases, no “jumps” are present. This robustness represents another advantage of the method. Fourth, the increasing synchrony suggested by spatiotemporal patterns, at four illustrative values of C , agrees well with the svM-SSA. Other features captured by the svM-SSA are present, but are out of the scope of the present work. The main message of the aforementioned results is that svM-SSA provides detailed information about the synchronization dynamics.

5.2 Hindmarsh-Rose model

In this section we consider a network of identical neuron models but with different initial conditions in a chain topology of $J = 5$ oscillators. The dynamical regime of such models ($I = 3.25$) lead to chaotic bursts (see Sec. 2.3).

Consider a set of HR neuron models coupled according to (Handa and Sharma, 2016)

$$\begin{cases} \dot{x}_j = y_j - ax_j^3 + bx_j^2 + I - z_j + g \sum_{i \in \Gamma_j} (x_i) \\ \dot{y}_j = c - dx_j^2 - y_j \\ \dot{z}_j = r[s(x_j - x_1) - z_j], \end{cases} \quad (25)$$

with $j = 1, \dots, J$, and Γ_j being the set of values of i that correspond to the oscillators coupled to j . Data was generated by integrating (25) with $(h, t_s, t_{\text{sim}}, t_{\text{trans}}) = (0.1, 0.1, 8500, 500)$ – for the svM-SSA, data was decimated by 10, yielding an effective $t_s = 1$ t.u. We set $(a, b, c, d) = (1, 3, 1, 5)$ and $I = 3.25$, in order to generate

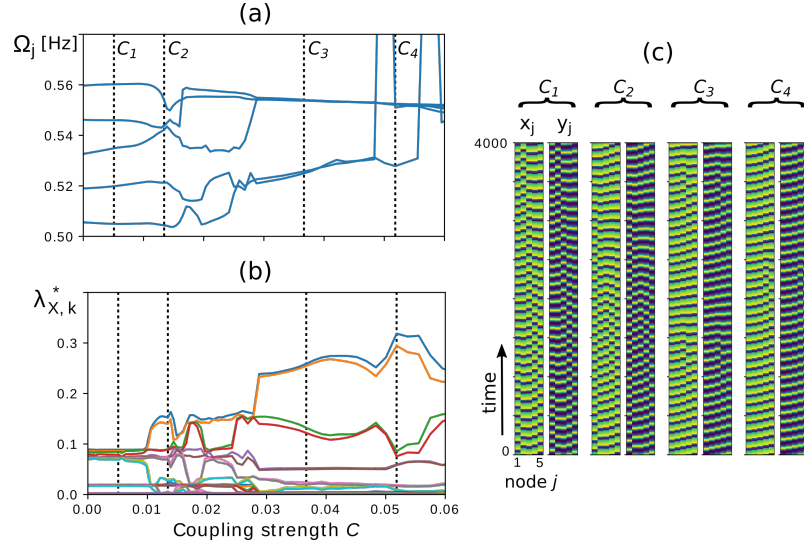


Figure 7: Phase synchronization analysis of $J = 5$ detuned FitzHugh-Nagumo neurons for an increasing coupling strength C . Four values of C (vertical dashed lines) were selected to guide the following analysis. Both the (a) mean observed frequencies Ω_j (linear fit of the phases estimated from the analytical signal) and the (b) svM-SSA show the PS clustering formation. But the latter (i) provides an early sign of PS and (ii) is not affected by phase slips as the former (as seen in the abrupt jumps of Ω_j at C_4). (c) A direct visual inspection of the x and y time series agrees with the results of these techniques, but its analysis is far less clear.

a “random” burst structure. Figure 8(a) shows that each neuron has a different bursting sequence for the coupling strength $g = 0$ (i.e., uncoupled).

The “period” of the fast time scale corresponds to the inter-spike interval in a burst, which is ≈ 15 data points (in the decimated time series). Hence, we set $m = 30$ following (Portes and Aguirre, 2016a). In doing so, a single high λ [Fig. 8(c)] is seen in the svM-SSA template. It is followed by a slowly decreasing tail of singular pairs, which correspond to the several time scales present in the signal [the PSD, 8(b), shows two of them]. Finally, we choose $S = 25$ eigenvectors of the structured-varimax rotation, which correspond to the 5 leading singular values of each single-neuron as its phase dynamics fingerprint (based on the template).

Figure 9 shows the results for 100 (logarithmically spaced) steps of an increasing synaptic coupling strength $g \in [0, 0.4]$. For $g \approx 0$, each neuron is represented by the corresponding leading λ_1 . Increasing g , a somewhat intermittent PS appears. Three values of g (vertical dashed lines), that reveal increasing PS, were selected. The respective time series, Fig. 9(b), confirm the increasing synchronization of the bursts. Note that the spikes themselves are not synchronized (as seen in the selected initial segments and in the respective raster plots). The two high singular values for $g = g_3$ indicate PS behavior of two dominant clusters. From the raster plots it is seen that such clusters are not fixed, in the sense that some neuron models synchronize intermittently with each of them. The detailed analysis of this intermittent PS behavior is left for future research.

5.3 Izhikevich’s spiking neuron model

As seen in the previous section, the svM-SSA is a powerful tool to provide information about phase synchronization dynamics, at least for *few* oscillators. But computational investigations on neuronal dynamics also include networks with a *massive* number of neurons such as $J \sim 10^3$ up to 10^6 and above. For example, a network model of the mammalian thalamocortical system exhibited polychronous activity only with $J > 10^4$ neurons (Izhikevich and Edelman, 2008).

Hence, in this section we explore what kind of information, if any, the svM-SSA can provide about synchronization dynamics in a large population of neuron models. To this end, a numerical experiment using a network with $J = 1000$ Izhikevich neuron models is reported. Such a model has both biological plausibility and computational efficiency, been able to emulate nearly 20 neuro-computational properties of biological spiking neurons and hence is adequate for this type of simulation studies (Izhikevich, 2004). The same rationale (parameters, integration method etc) of the original work (Izhikevich, 2003) was followed, unless otherwise stated.

We investigate the synchronizability of the network in function of the coupling

strength. This is done by manipulating the synaptic current (I_{syn}) with an scaling factor (coupling gain) $g \in [0, 1]$. This is implemented by splitting the input current term in (4) as $I^j = I_{\text{in}}^j + gI_{\text{syn}}^j$ (being I_{in} the injected dc-current, and $j = 1, \dots, J$ the neuron index). The *same* randomly generated synaptic weight matrix was used in all simulations, as well the number of excitatory ($N_e = 800$) and inhibitory ($N_i = 200$) neurons. For a given value of g , the *spike raster* time series were generated with $(h, t_s, t_{\text{sim}}, t_{\text{trans}}) = (1, 1, 1000, 0)$ (ms time units). Figure 10(a-c) shows a representative example for $g = 1$, along with the respective local field potential. One hundred values of g were used, equally spaced in the aforementioned range.

Note that the relevant dynamical information is coded in the inter-spike interval (ISI), and not in their magnitude. In view of this, the raster time series from $v(t)$ is used in order to decrease the computational load from the augmented trajectory matrix. Following (Portes and Aguirre, 2016a) for the svM-SSA of the Hindmarsh-Rose neuron model (see Sec. 5.2), the window width was chosen as $m = 4$, that results in a window length of $4 \times t_s = 4$ ms, which is four times larger than the fast time scale (1 ms of the spike duration). For the structured varimax rotation only the $S = 2J = 2000$ leading singular vectors were used which requires the rotation of a matrix of size 2000×2000 .¹

The svM-SSA spectrum for the increasing coupling gain g is shown in Fig. 11(a). The behavior and quantity of the λ_k^* render the plot complicated and no *specific* phase synchronized cluster information is clear seen. On the other hand, a *general* picture of the synchronization dynamics is provided if one focuses on $\lambda_{1,2}^*$ (the leading pair), corresponding to the stronger, global, oscillatory mode present in the data. The following features are worth mentioning. First, there is a clear overall growing trend of $\lambda_{1,2}^*$ values for increasing gain g (marked by the gray thick lines). Second, the spectrum suggests that no global PS emerges until $g \approx 0.5$, where the slope of the aforementioned trend starts to increase. The insets in Fig. 11(a) show the spike raster and respective local field potential (LFP), for two representative values of $g < 0.4$, with no clear visible sign of synchronized spiking. Third, higher values of g do not necessarily imply a “higher level” of PS, as shown by the presence of high peaks (higher level of PS) surrounded by deep valleys (lower level of PS). As a cross-check, the raster spikes and respective LFP at and around the two selected peaks at $\{g^*, g^{**}\} = \{0.6868, 0.9292\}$ are shown in Figs. 11(b, c), respectively. Both

¹This is done for two reasons. First, in order to minimize computational effort, since the structured varimax rotation algorithm (Portes and Aguirre, 2016b) is based on a singular value decomposition (SVD), which is known to have a time complexity of order $O[\min(pq^2, p^2q)]$ for a generic matrix of size $p \times q$ (i.e., $O(2000^3)$ in the present case). Second, to simplify the analysis of the svM-SSA spectrum by following just one oscillatory mode per system, corresponding to two singular values λ_k .

ranges show signatures of synchronization, which is more visible near the second (and higher) peak at $g = g^{**}$ [Figs. 11(c)]. Hence in the context of a large network, the svM-SSA is still able to provide the general picture of PS.

6 Conclusions

In most studies involving neuron models, it is common to use the first state variable – the membrane potential – for monitoring or controlling purposes. This choice of variable results from the fact that, in experimental neuron network, only this variable can be actually measured. However, it is important, from a theoretical point of view, to know if such a choice is the most adequate in terms of the dynamical behavior.

One of the objectives of this paper has been to investigate observability properties of neuron models. This has been done using three different quantifiers for observability: coefficients determined numerically from the model equations (Letellier et al., 2005), from data (Aguirre and Letellier, 2011) or symbolic coefficients analytically obtained from the model equations (Letellier and Aguirre, 2009). This procedure turned out to reveal the limitations of some techniques, for instance, due to the complexity of the equations and the physical interpretation of the variables, investigating the observability of the Hodgkin-Huxley model is viable only using the data-estimated SVDO coefficients or the symbolic observability coefficients. Also, the performance of such a method using discontinuous data as for Izhikevich’s spiking neuron model is uncertain. This mostly results from the fact that in this latter model, the switching mechanism is not fully described by the equations and there is at least one missing variable in the model for having a complete description of the underlying mechanisms. Observability is therefore investigated from a truncated model and it remains an open question how to assess observability in such discontinuous systems.

In summary the variables that convey greater observability were: the membrane potential in the Hodgkin-Huxley and Izhikevich’s models (especially in the chattering regime), whereas for FitzHugh-Nagumo the observability provided by the potential and recovery variables is comparable. In this respect, the Hindmarsh-Rose model has some peculiarities in what concerns observability. The membrane potential and fast recovery variable reveal the fast time scales such as the spikes in the chattering regime, whereas the z variable (slow recovery) is the only one to clearly reveal the chaotic nature of the dynamics when it occurs.

We also investigated some of the aforementioned models in the context of synchronization. In particular, networks formed of five phase coherent FitzHugh-Nagumo neurons, five bursting Hodgkin-Huxley neurons, and one with 1000 Izhike-

vich neurons were analyzed. A technique known as structured-varimax multivariate singular spectrum analysis, from a variable that provides good observability of the dynamics, was used to successfully detect phase synchronization in the networks. Two interesting features of this technique is that it does not require computing the phase and it is able to detect synchronization in situations where other methods give an unclear indication.

Acknowledgements

The authors gratefully acknowledge financial support from Conselho Nacional de Desenvolvimento Científico e Tecnológico (CNPq), Brazil.

References

- Aguirre, L. A. (1995). A nonlinear correlation function for selecting the delay time in dynamical reconstructions. *Phys. Lett.*, 203A(2,3):88–94.
- Aguirre, L. A. and Letellier, C. (2005). Observability of multivariable differential embeddings. *J. Phys. A: Math. Gen.*, 38:6311–6326.
- Aguirre, L. A. and Letellier, C. (2011). Investigating observability properties from data in nonlinear dynamics. *Physical Review E*, 83(066209).
- Belykh, I., De Lange, E., and Hasler, M. (2005). Synchronization of bursting neurons: What matters in the network topology. *Phys. Rev. Lett.*, 94(188101).
- Bianco-Martinez, E., Baptista M. S., and Letellier, C. (2015). Symbolic computations of nonlinear observability. *Physical Review E*, 91 (062912).
- Broomhead, D. S. and King, G. P. (1986). Extracting qualitative dynamics from experimental data. *Physica D*, 20:217–236.
- Brown, J. W. (2014). The tale of the neuroscientist and the computer: why mechanistic theory matters. *Frontiers in Neuroscience*, 8:349.
- FitzHugh, R. (1961). Impulses and physiological states in theoretical model of nerve membrane. *Biophysical Journal*, 1:445–466.
- Friedland, B. (1975). Controllability index based on conditioning number. *Journal of Dynamic Systems, Measurement, and Control*, 97(4):444–445.

- Frunzete, M., Barbot, J. P., and Letellier, C. (2012). Influence of the singular manifold of nonobservable states in reconstructing chaotic attractors. *Phys. Rev. E*, 86(2):026205.
- Girardi-Schappo, M., Tragtenberg, M. H. R., and Kinouchi, O. (2013). A brief history of excitable map-based neurons and neural networks. *Journal of Neuroscience Methods*, 220:116–130.
- Groth, A. (2015). Monte Carlo singular spectrum analysis (SSA) revisited: Detecting oscillator clusters in multivariate datasets. *Journal of Climate*, 28(19):7873–7893.
- Groth, A. and Ghil, M. (2011). Multivariate singular spectrum analysis and the road to phase synchronization. *Phys. Rev. E*, 84(036206).
- Handa, H. and Sharma, B. B. (2016). Synchronization of a set of coupled chaotic FitzHugh-Nagumo and Hindmarsh-Rose neurons with external electrical stimulation. *Nonlinear Dynamics*, 85(3):1517–1532.
- Hermann, R. and Krener, Arthur, J. (1977). Nonlinear controllability and observability. *IEEE Trans. Automat. Contr.*, 22(5):728–740.
- Hindmarsh, J. L. and Rose, R. M. (1984). A model of neuronal bursting using three coupled first order differential equations. *Proc. R. Soc. London*, B 221:87–102.
- Hodgkin, A. L. and Huxley, A. F. (1952). A quantitative description of membrane current and its application to conduction and excitation in nerve. *Journal of Physiology*, 117:500–544.
- Isidori, A. (1995). *Nonlinear Control Systems*. Springer, London.
- Izhikevich, E. M. (2003). Simple model of spiking neurons. *IEEE Transactions on Neural Networks*, 14(6):1569–1572.
- Izhikevich, E. M. (2004). Which model to use for cortical spiking neurons? *IEEE Transactions on Neural Networks*, 15(5):1063–1070.
- Izhikevich, E. M. and Edelman, G. M. (2008). Large-scale model of mammalian thalamocortical systems. *PNAS*, 105(9):3593–3598.
- Kalman, R. E. (1960). On the general theory of control systems. In *Proc. First IFAC Congress Automatic Control*, pages 481–492, London. Butterworths.
- Letellier, C. and Aguirre, L. A. (2002). Investigating nonlinear dynamics from time series: the influence of symmetries and the choice of observables. *Chaos*, 12(3):549–558.

- Letellier, C. and Aguirre, L. A. (2009). Symbolic observability coefficients for univariate and multivariate analysis. *Physical Review E*, 79(066210).
- Letellier, C., Aguirre, L. A., and Maquet, J. (2005). Relation between observability and differential embeddings for nonlinear dynamics. *Physical Review E*, 71(066213).
- Letellier, C., Maquet, J., Le Sceller, L., Gouesbet, G., and Aguirre, L. A. (1998). On the non-equivalence of observables in phase-space reconstructions from recorded time series. *J. of Phys. A*, 31:7913–7927.
- Letellier, C. Sendiña-Nadal, I., Bianco-Martinez, E., and Baptista, M. S. (2017). Assessing observability of reaction networks by using nonlinear symbolic coefficients. preprint.
- Lowet, E., Roberts, M. J., Bonizzi, P., Karel, J., and De Weerd, P. (2016). Quantifying neural oscillatory synchronization: A comparison between spectral coherence and phase-locking value approaches. *PLoS ONE*, 11(e0146443).
- Nagumo, J., Arimoto, S., and Yoshizawa, S. (1962). An active pulse transmission line simulating nerve axon. *Proc. IRE*, 50(10):2061–2070.
- Portes, L. L. and Aguirre, L. A. (2016a). Enhancing multivariate singular spectrum analysis for phase synchronization: The role of observability. *Chaos*, 26(093112).
- Portes, L. L. and Aguirre, L. A. (2016b). Matrix formulation and singular-value decomposition algorithm for structured varimax rotation in multivariate singular spectrum analysis. *Physical Review E*, 93(052216).
- Schiff, S. J. (2012). *Neural Control Engineering*. The MIT Press, Cambridge, Massachusetts.
- Sedigh-Sarvestani, M., Schiff, S. J., and Gluckman, B. J. (2012). Reconstructing mammalian sleep dynamics with data assimilation. *PLoS Comput Biol*, 8(11):e1002788.
- Sendiña-Nadal, I., Boccaletti, S., and Letellier, C. (2016). Observability coefficients for predicting the class of synchronizability from the algebraic structure of the local oscillators. *Phys. Rev. E*, 94(042206).
- Siettos, C. and Starke, J. (2016). Multiscale modeling of brain dynamics: from single neurons and networks to mathematical tools. *WIREs Syst Biol Med*, 8:438–458.

- Su, F., Wang, J., Li, H., Deng, B., Yu, H., and Liu, C. (2017). Analysis and application of neuronal network controllability and observability. *Chaos*, 27(023103).
- Voos, H. U., Timmer, J., and Kurths, J. (2004). Nonlinear dynamical system identification from uncertain and indirect measurements. *Int. J. Bifurcation and Chaos*, 14(6):1905–1933.

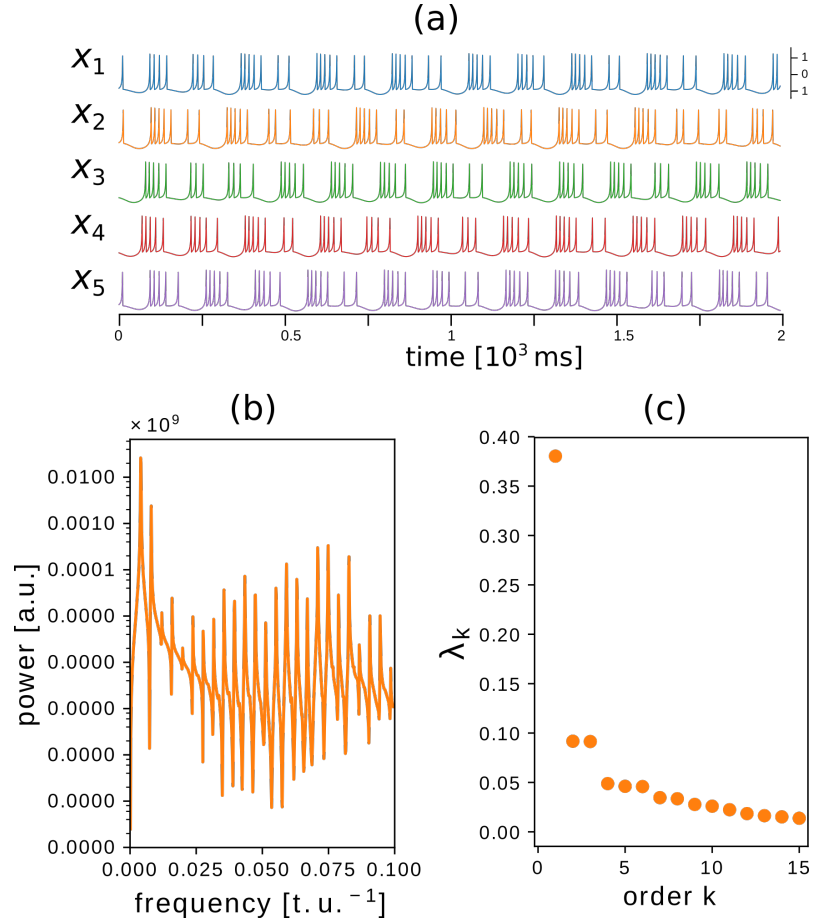


Figure 8: (a) x time series of the (*uncoupled*) $J = 5$ simulated Hindmarsh-Rose neurons show the generated “random” bursting structures. For a given oscillator, the (b) PSD shows two dominant low frequencies (from the slow oscillatory mode), and the (c) template for the svM-SSA displays a “drift” signature (leading isolated λ_1 , see text) and a slowly decreasing tail of singular value pairs corresponding to the several oscillatory modes present in the signal.

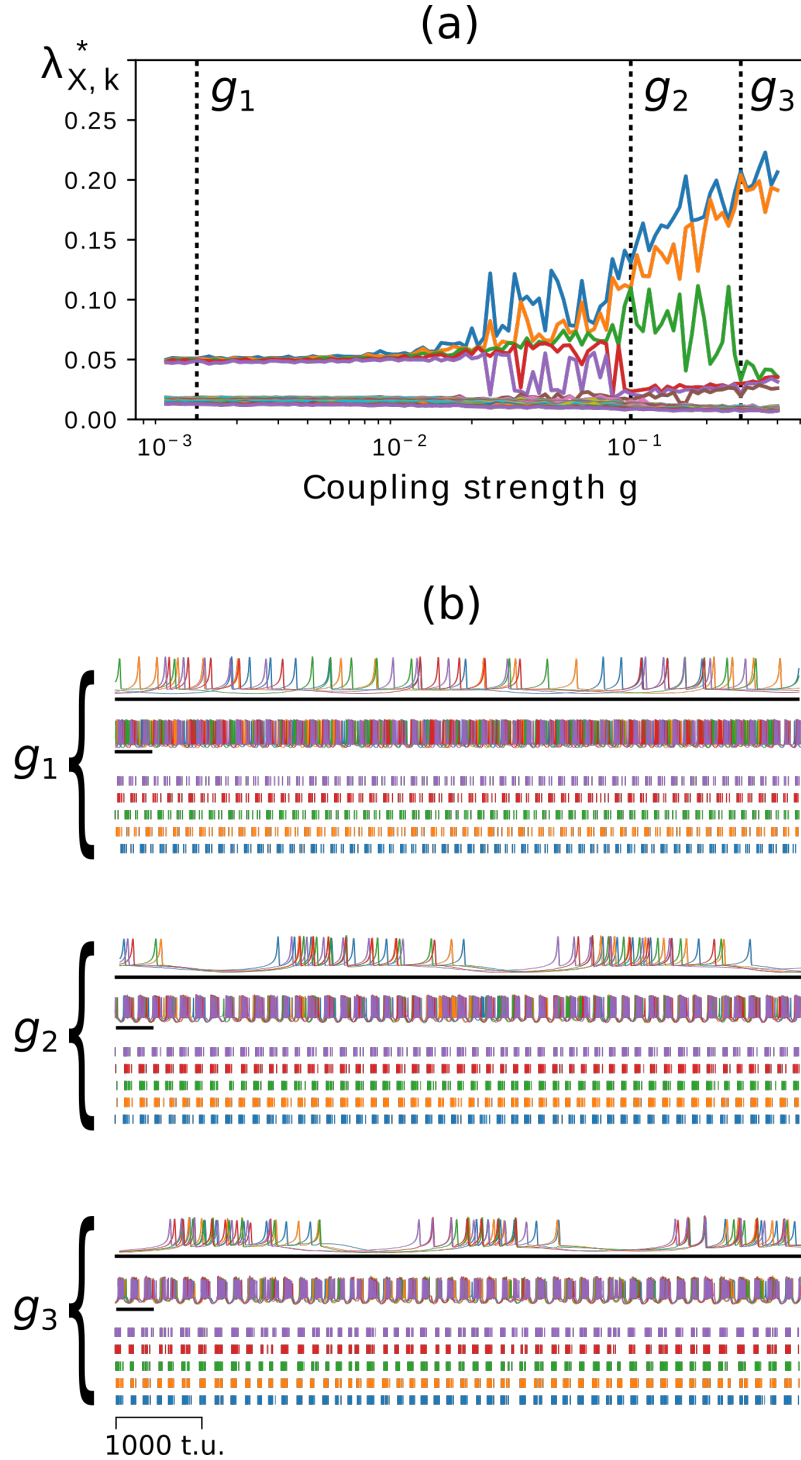


Figure 9: Synchronization analysis of $J = 5$ Hindmarsh-Rose neurons coupled in a chain, for an increasing synaptic coupling strength g . (a) the svM-SSA shows the PS dynamics. For $g \approx 0$, each bursting neuron is identified by its single leading λ_k (as suggested by the template analysis, see text). Increasing g , the spectrum suggests an increasing synchronization due the formation of PS clusters. (b) the x time series at three selected values of g (vertical dashed lines), along with a “zoom” view of the initial segment, show an increasing tendency to synchronization, in agreement with the svM-SSA results. Intermittent synchronization can be seen in the raster plots.

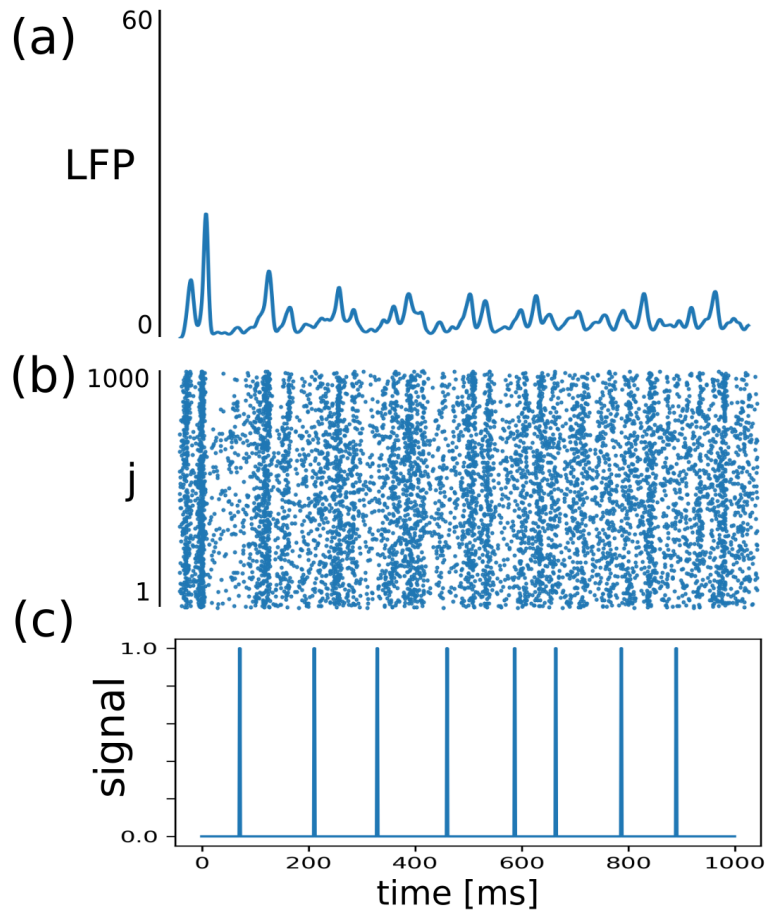


Figure 10: Simulation results for $g = 1$. (b) Spike raster and (a) its respective local field potential, showing signatures of spiking synchronization. (c) Typical spike raster signal, obtained from neuron $j = 1$.

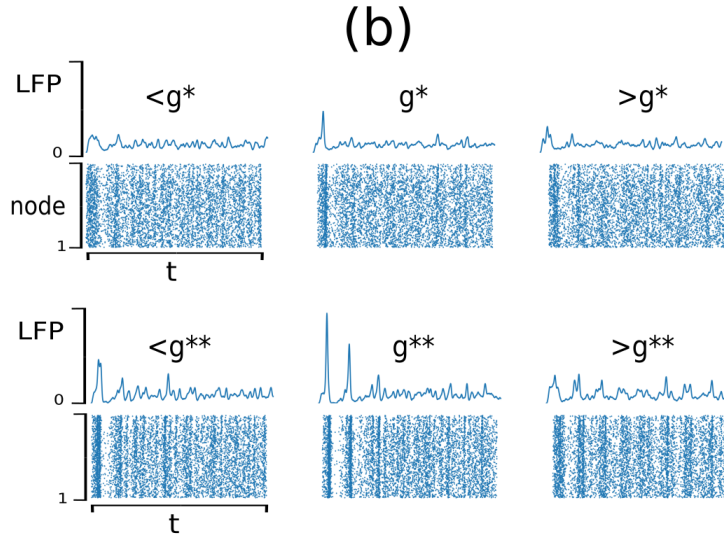
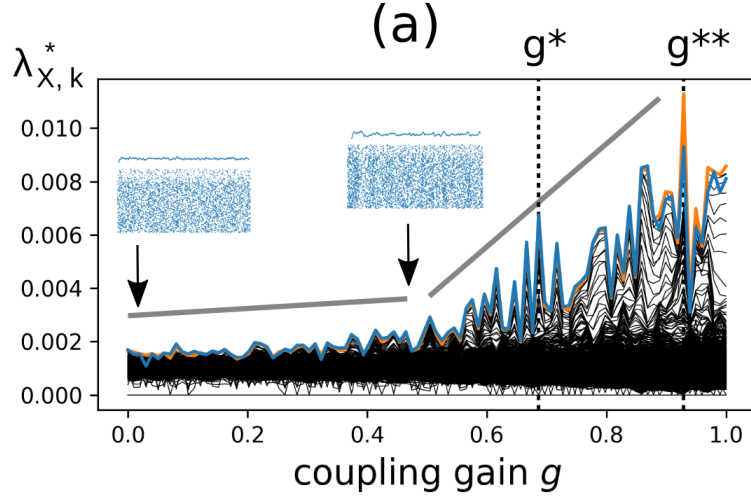


Figure 11: (a) (a) Modified singular values $\lambda_{Y,k}^*$ for $N = 1000$ pulse-coupled Izhikevich neuron models for an increasing inter-neuron coupling gain g . The two thick (blue and orange) lines correspond to the highest singular values, $\lambda_{1,2}^*$. The increasing in synchronicity, for larger values of g , have a higher slope (thick gray lines) for $g > 0.5$. The insets illustrate typical spike raster plots (SRP) and their respective local field potential (LFP) found for $g < 0.5$. No clear signature of synchronicity is seen, which agrees with the low values of λ_k for this range of g . Two high peaks in the svM-SSA spectrum (g^* and g^{**}), suggesting PS, were selected for closer inspection. Their respective LFP and SRP, along with the ones for the surrounding values of g , are shown in (b). They show a clear sign of synchronism, which is stronger near g^{**} than near g^* , in agreement with the svM-SSA spectrum.